



# Global Biogeochemical Cycles

## RESEARCH ARTICLE

10.1029/2018GB006045

### Key Points:

- The Zn:PO<sub>4</sub><sup>3-</sup> uptake ratio varies by approximately tenfold across latitude and is modulated by Fe availability
- Zn remineralizes similar to PO<sub>4</sub><sup>3-</sup> in the upper ocean, but its accumulation in deep waters exceeds that of PO<sub>4</sub><sup>3-</sup>
- The strong Zn-SiO<sub>4</sub><sup>4-</sup> correlation is caused by a combination of surface uptake, desorption from particles, and hydrothermal input

### Supporting Information:

- Supporting Information S1

### Correspondence to:

S. Roshan,  
sroshan@ucsb.edu

### Citation:

Roshan, S., DeVries, T., Wu, J., & Chen, G. (2018). The internal cycling of zinc in the ocean. *Global Biogeochemical Cycles*, 32, 1833–1849. <https://doi.org/10.1029/2018GB006045>

Received 30 JUL 2018

Accepted 3 DEC 2018

Accepted article online 7 DEC 2018

Published online 28 DEC 2018

## The Internal Cycling of Zinc in the Ocean

Saeed Roshan<sup>1,2</sup> , Tim DeVries<sup>1,2</sup> , Jingfeng Wu<sup>3,4</sup> , and Gedun Chen<sup>4</sup>

<sup>1</sup>Department of Geography, University of California, Santa Barbara, CA, USA, <sup>2</sup>Earth Research Institute, University of California, Santa Barbara, CA, USA, <sup>3</sup>College of Life Science and Oceanography, Shenzhen University, Shenzhen, China, <sup>4</sup>Rosenstiel School of Marine and Atmospheric Science, University of Miami, Coral Gables, FL, USA

**Abstract** The internal cycling of zinc (Zn) in the ocean has been a longstanding mystery. Particularly, puzzling is the strong correlation between Zn and silicate (SiO<sub>4</sub><sup>4-</sup>), but not phosphate (PO<sub>4</sub><sup>3-</sup>), even though Zn is involved with cell functions that regulate PO<sub>4</sub><sup>3-</sup> uptake and are unrelated to SiO<sub>4</sub><sup>4-</sup> uptake. To help solve this mystery, we use an artificial neural network to produce global maps of dissolved Zn, and then use a diagnostic model to infer rates of uptake and regeneration for Zn, SiO<sub>4</sub><sup>4-</sup>, and PO<sub>4</sub><sup>3-</sup>. We find that plankton in the Southern Ocean account for 62 (±32)% of global Zn uptake. The plankton Zn:PO<sub>4</sub><sup>3-</sup> uptake ratio increases by more than tenfold from the low latitudes to the Southern Ocean, a much larger range than expected from culture studies, suggesting controls from factors such as iron availability. Reconstruction of particulate Zn (PZn), phosphorus (PP), and biogenic silica (PSi) fluxes reveals that PZn remineralizes like PP, and not like PSi. However, a small flux of PZn into the deep ocean is not matched by an equivalent flux of PP, which is likely due to the combined effects of desorption of scavenged Zn and the input of hydrothermal Zn in the deep ocean. This small difference in the remineralization of PZn and PP, combined with the patterns of surface uptake, eliminates the correlation between Zn and PO<sub>4</sub><sup>3-</sup> in the deep ocean and causes a tight correlation between Zn and SiO<sub>4</sub><sup>4-</sup>. This coincidental correlation cannot be expected to hold for past and future states of the ocean.

**Plain Language Summary** Marine phytoplankton account for half of global net primary production. These plankton require zinc (Zn) to grow, but the cycle of Zn in the ocean is not well understood. We combined observations and a model to determine that plankton use Zn at highly variable rates, with lowest rates in the tropical oceans and highest rates in the Southern Ocean. This bioassimilated Zn reenters water column as swiftly as phosphorous. However, Zn is enriched relative to phosphorous in the deep ocean due to additional inputs of Zn from seafloor hydrothermal vents, and from desorption of Zn that has been scavenged onto sinking particles. These processes cause the hitherto mysterious correlation between Zn and silicon, an element not involved in the Zn cycle.

## 1. Introduction

Crucial biological functions have been identified for zinc (Zn) in the growth of the oceanic plankton (Anderson & Morel, 1978; Brand et al., 1983). These biological roles are linked to vital processes such as assimilation of dissolved inorganic carbon and organic phosphorus and utilization of gene-encoded information (Twining & Baines, 2013). These roles establish a connection between the cycles of Zn and other essential nutrients and might explain the nutrient-type distribution of oceanic Zn: depleted in the surface ocean through biological uptake and accumulated in the deep ocean through decomposition of organic matter (Bruland et al., 2014). However, comparing dissolved Zn and macronutrient distributions reveals that the subsurface accumulation of Zn occurs deeper than that of macronutrients associated with plankton soft tissues (i.e., phosphate) and coincides with silicate, which is the building block of diatom frustules (Figure 1a; Bruland, 1980; Wyatt et al., 2014; Roshan & Wu, 2015). This results in a paradox since the known Zn biological functions and Zn bioaccumulation are associated with soft (organic) tissues, rather than the siliceous frustules of diatoms (Ellwood & Hunter, 2000; Twining & Baines, 2013).

Two hypotheses have been proposed to resolve this paradox. The first proposes that Zn and silicate (SiO<sub>4</sub><sup>4-</sup>) are preferentially incorporated by diatoms (albeit in different tissues) relative to phosphate (PO<sub>4</sub><sup>3-</sup>) in the Southern Ocean, leading to an accumulation of regenerated Zn and SiO<sub>4</sub><sup>4-</sup> in the deep Southern Ocean water masses (de Souza et al., 2018; Croot et al., 2011; Vance et al., 2017). In this hypothesis, Zn and

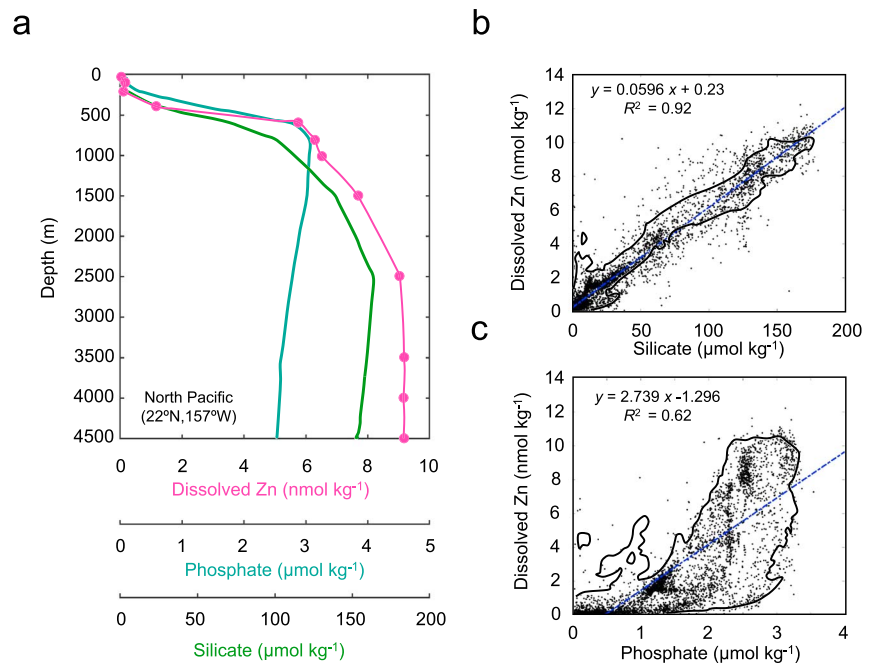


**Figure 1.** Comparison between dissolved Zn,  $\text{SiO}_4^{4-}$ , and  $\text{PO}_4^{3-}$  distributions. (a) Vertical distributions of dissolved Zn,  $\text{SiO}_4^{4-}$ , and  $\text{PO}_4^{3-}$  in the North Pacific Ocean. Observed dissolved Zn concentrations are plotted against observed (b)  $\text{SiO}_4^{4-}$  and (c)  $\text{PO}_4^{3-}$ . Least squares regressions are shown as dashed blue lines. The black contours in panels b and c are drawn at 1% of the maximum likelihood of our artificial neural network (ANN)-derived dissolved Zn climatology compared to climatological  $\text{SiO}_4^{4-}$  and  $\text{PO}_4^{3-}$  concentrations. These contours contain 85% and 97% of the climatological Zn- $\text{SiO}_4^{4-}$  and Zn- $\text{PO}_4^{3-}$  pairs, respectively, and 83% and 93% of observational Zn- $\text{SiO}_4^{4-}$  and Zn- $\text{PO}_4^{3-}$  pairs, respectively, demonstrating good agreement between the climatologies and raw data.

$\text{SiO}_4^{4-}$  are regenerated with different length scales, but become correlated through vigorous vertical mixing of the Southern Ocean's subsurface water masses. Mixing of these Zn- and  $\text{SiO}_4^{4-}$ -enriched waters with the rest of the ocean establishes the global dissolved Zn- $\text{SiO}_4^{4-}$  correlation (Vance et al., 2017; Figure 1b). A neglected point in this hypothesis is that subsurface regeneration outside the Southern Ocean (north of 40°S) is responsible for >85% of the  $\text{SiO}_4^{4-}$  occurring in that region and ~38% of the global regenerated  $\text{SiO}_4^{4-}$  (Holzer et al., 2014). Thus, processes outside the Southern Ocean must also play a role in establishing the correlation of Zn against  $\text{SiO}_4^{4-}$ . A second hypothesis suggests that in addition to regeneration, Zn is also scavenged onto sinking particles, similar to other particle-reactive trace metals (Bruland et al., 1994; John & Conway, 2014; Weber et al., 2018). Desorption of particle-scavenged Zn further down in the water column leads to an accumulation of dissolved Zn in the deep ocean, coincident with the deep dissolution of biogenic Si (Weber et al., 2018). This equilibrated adsorption-desorption mechanism is termed reversible scavenging (Bacon & Anderson, 1982; John & Conway, 2014; Weber et al., 2018).

To better understand the internal cycling of Zn in the ocean, we compile a global database of high-quality dissolved Zn data and use an artificial neural network (ANN) technique to produce a global climatology of dissolved Zn concentration (climatology is publically available in Roshan et al., 2018). Climatologies of hydrographic data and nutrients are usually constructed using interpolation methods that only consider spatial (and rarely temporal) features (e.g., Lauvset et al., 2016; Locarnini et al., 2013). Such methods would certainly fail for the case of dissolved Zn, due to the sparsity of spatial coverage (Figure S1 in the supporting information). In addition to spatial features such as depth, latitude, and longitude, the ANN is able to use other features such as climatologies of physical and biogeochemical tracers. The ANN is trained to recognize the relationship between these *input* features (complete list in section 2.1) and the *output* of the network, in this case the concentration of dissolved Zn (sections 2.2–2.4). In this way, the physical and biogeochemical information contained in previously mapped climatologies is leveraged to produce a global climatology of

dissolved Zn (section 3.1). The ANN uses data subsampling to ensure appropriate extrapolation, and we use an ensemble of ANNs to provide a measure of uncertainty arising from sparse data coverage.

We then assimilate this climatology, along with existing climatologies of  $\text{SiO}_4^{4-}$  and  $\text{PO}_4^{3-}$ , into a diagnostic model that estimates rates of dissolved Zn,  $\text{SiO}_4^{4-}$ , and  $\text{PO}_4^{3-}$  uptake and regeneration (sections 3.2–3.3). This diagnostic model provides an estimate of Zn and macronutrient cycling that is optimally consistent with available observations and avoids errors associated with prognostic modeling, such as parameter misspecification or incorrect model formulation (Roshan & DeVries, 2017; Weber et al., 2016). Using this approach, we reconstruct a complete picture of the internal cycling of Zn and its relation to those of phosphorus and silicon in the ocean (section 3.4). We offer concluding remarks in section 4.

## 2. Methods

The methodology of this study consists of (i) developing an ensemble of ANNs to produce climatological maps of dissolved Zn with the same spatial resolution as the World Ocean Atlas 2013 (WOA13; <https://www.nodc.noaa.gov/OC5/woa13/>;  $1^\circ \times 1^\circ \times 102$  depth levels) and (ii) coupling these dissolved Zn maps, and those of  $\text{PO}_4^{3-}$  and  $\text{SiO}_4^{4-}$  from WOA13, to a data-constrained ocean circulation model, and employing a restoring model to compute the biogeochemical sources and sinks of dissolved Zn,  $\text{PO}_4^{3-}$ , and  $\text{SiO}_4^{4-}$ . The following sections detail the different steps of our method.

### 2.1. ANN Settings

An ANN is a machine learning technique inspired by biological neural systems (Hassoun, 1995). In general terms, an ANN simulates output(s) from input feature(s) given a set of trainable parameters that connect input layers to one or more *hidden layers* of the ANN. Optimal parameters are determined by training the ANN to reproduce a set of known outputs from the set of input features. Once the optimal parameters are determined, the ANN can be used to simulate outputs for instances where inputs exist but outputs do not. This makes the ANN ideal for interpolations of sparse oceanographic data (e.g., Roshan & DeVries, 2017; Sauzède et al., 2017). The reader is referred to standard texts on the subject for further details (e.g., Hassoun, 1995).

The ANNs applied in this study consist of one input layer assimilating 16 input features: temperature, salinity, oxygen, apparent oxygen utilization, phosphate, nitrate, silicate,  $\delta^3\text{He}$  (deviation of  $^3\text{He}/^4\text{He}$  isotope ratio from that of the atmosphere), chlorophyll, depth of photic zone, potential density anomaly ( $\sigma_\theta$ ), and spatial variables such as sampling depth,  $\sin(\text{latitude})$ ,  $\cos(\text{latitude})$ ,  $\sin(\text{longitude})$ , and  $\cos(\text{longitude})$ . The input layer is fully connected, in a feedforward fashion, to a single hidden layer consisting of 10, 15, 20, or 25 neurons (the number of neurons was chosen randomly in each ANN model setup and training). A sigmoidal function is applied to the hidden layer, and the result is connected to a single-node output layer. We apply a rectifier function to the output layer to avoid negative output (Figure S1). A Levenberg-Marquardt algorithm was used to train the ANNs, where the objective is to minimize the mean square error between the output (ANN-predicted dissolved Zn) and the target (observed dissolved Zn). A schematic of the ANN applied in this study is shown in Figure S1.

### 2.2. Dissolved Zn Data

A dissolved Zn data set is compiled mostly from the GEOTRACES Intermediate Data Product (2017 version; Mawji et al., 2015; Schlitzer et al., 2018), most of which are also published individually (Croot et al., 2011; Janssen & Cullen, 2015; John et al., 2018; Kim et al., 2017; Roshan et al., 2016; Roshan & Wu, 2015; Wyatt et al., 2014), plus several pre-GEOTRACES data sets (Bruland, 1980; Fitzwater et al., 2000; Martin et al., 1989; Martin et al., 1993). Overall, the samples were collected from 1977 to 2013, mostly in spring/summer, and their locations are shown in Figure S2. For this study, we also measure Zn along a meridional section in the tropical-subtropical North Pacific (blue circles in Figure S2), using a method described elsewhere (Roshan et al., 2016; Roshan & Wu, 2015). Temperature, salinity, oxygen, apparent oxygen utilization, phosphate, nitrate, and silicate global climatological fields are obtained from World Ocean Atlas 2013 (version 2; Locarnini et al., 2013; Zweng et al., 2013; Garcia et al., 2014a, 2014b).  $\delta^3\text{He}$  data are simulated by an ocean circulation model (DeVries, 2014) and optimized to best reproduce the observed  $\delta^3\text{He}$ . Surface maps of chlorophyll concentration (determined by SeaWiFS) are downloaded from <http://www.>

science.oregonstate.edu/ocean.productivity/index.php for the time-span of 1997 to 2009 and time-averaged. The depth of the photic zone is calculated using the time-averaged chlorophyll map and previously established relationships (Morel et al., 2007).  $\sigma_\theta$  is calculated from the equation of state of seawater.

### 2.3. Data Quality Control

Some of the available dissolved Zn data are not used in our study due to various issues. We excluded Zn observations from a transect in the Mediterranean and Black Seas (transect GA04; shown as purple circles in Figure S2), since relationships specific to this region might lead to biases in our model which seeks to describe open-ocean regions (see discussion in the following section). Data presented by Croot et al. (2011) within the Atlantic sector of the Southern Ocean, along GIPY05 (see Figure S2) have been demonstrated to be too low, and thus, we use the data produced by Zhao et al. (2014) for this section. The transect GPpr02 in the Southern Ocean south of Australia (Figure S2) has a large number of data points with negative values (Schlitzer et al., 2018), which might have arisen from an incorrect blank determination, and therefore, we do not use these data. The GIPY06, GIPY02, and GPpr01 data (Figure S2) were also produced using a similar method and thus are also excluded. Data reported for the Ross Sea (Fitzwater et al., 2000) are of unknown quality, and thus, we include these data in only half of the ANNs. We tested the ANN model with and without these excluded data and found that the model performance is much better without the excluded data (Figure S3), which is further evidence that these data are of lower quality and should be excluded.

### 2.4. Supervising the ANN

A large number of ANNs are set up and trained, from which 100 ANNs are chosen based on their performance against a test subset of observations. The test subset consists of a randomly chosen 30% of the dissolved Zn data set that remains unseen during model training, along with three high-quality full-depth profiles and a surface transect in the Southern Ocean (Zhao et al., 2014). In other words, the ANNs are trained (or optimized; see Figure S1 for optimization parameters) and benchmarked against 70% and 30% (plus the aforementioned Southern Ocean data) of the compiled data set, respectively. These training and test subsets are resampled for each ANN, as is the number of hidden neurons, such that each ANN generalizes differently from the others. By producing an ensemble of 100 ANNs using different random test subsets and numbers of neurons, we obtain an estimate of the uncertainty in the Zn climatology resulting from both the sparse spatiotemporal coverage of the dissolved Zn observations (Figure S2) and from the degrees of freedom that the ANN is given in order to match the Zn observations.

The model performance is quantified by calculating  $R^2$  between the observed Zn in the test subset and that predicted by the trained ANN. ANNs are kept if they yield  $R^2 > 0.95$  on the randomly excluded test subset,  $R^2 > 0.95$  on the three Southern Ocean profiles, and  $R^2 > 0.8$  on the surface Southern Ocean data. This supervision prevents issues of overfitting and noise in the model results and also ensures that the model generalizes well, particularly in the critical Southern Ocean region. The ANN model ensemble is able to reproduce unseen observations very well, with an  $R^2$  of 0.96 and root-mean-square error of 0.62 nmol/kg (Figure S4a). Profiles at individual stations also display a very good fit to observations, with  $R^2$  on individual profiles ranging from 0.89 to 1.00 (Figure S5). Since dissolved Zn is tightly correlated with  $\text{SiO}_4^{4-}$ , it might be thought that the ANN models build their consciousness patterns only around this correlation. However, we find that the ANNs are able to effectively recognize and match the small deviations from this correlation (Figure S4b).

We note that the dissolved Zn data collected at different times were binned into a single spatial grid (i.e., that of WOA;  $1^\circ \times 1^\circ \times 102$  depth levels) that neglects temporal (e.g., seasonal) variability. Likewise, the input nutrient and hydrographic features are from the annual mean climatologies. Thus, there may be some inconsistency between the Zn data and the input features, if the Zn data are not representative of annual mean conditions. Because each of our 100 ANNs is trained on random selections of data points, where the average collection time varies in different training and test subsets, this inconsistency is propagated to uncertainty in the final ANN-produced dissolved Zn climatology, which we consider the annual mean.

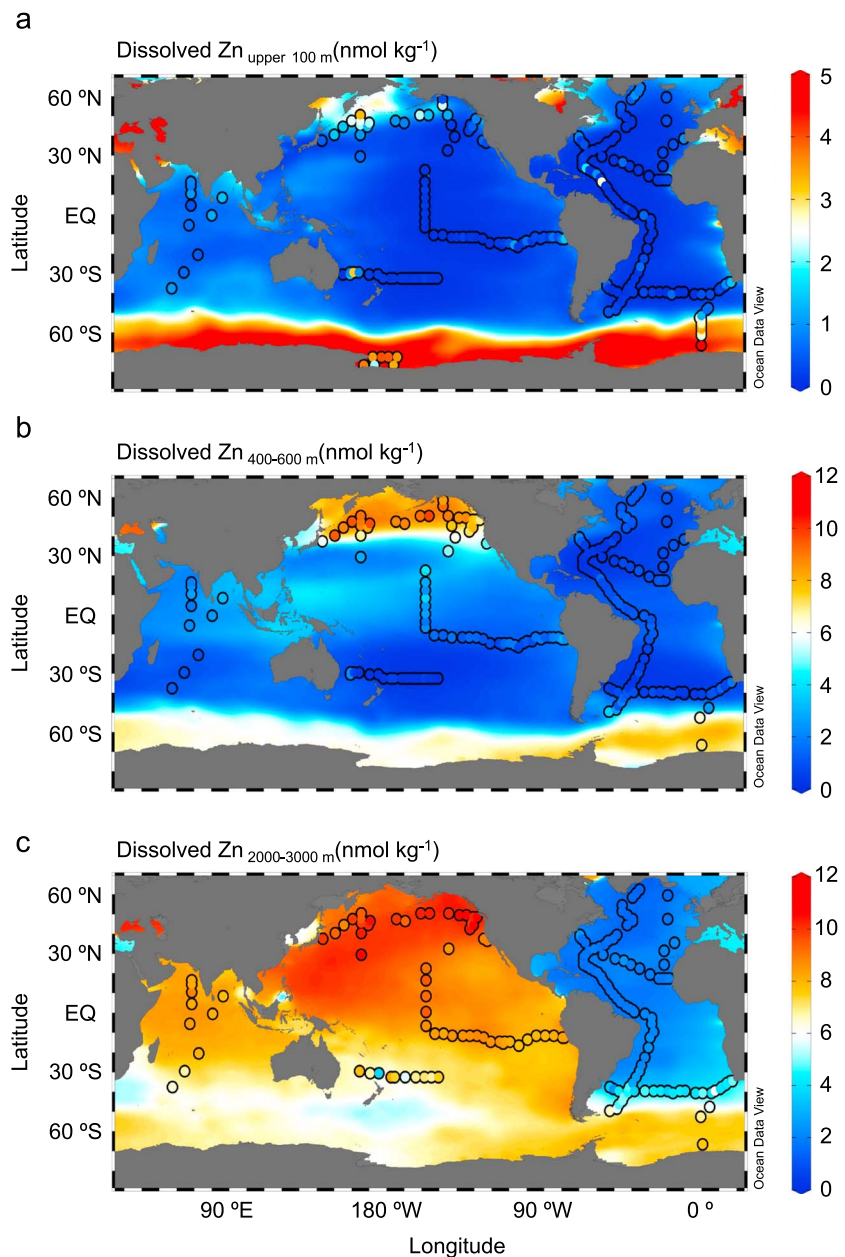


**Figure 2.** Horizontal distributions of dissolved Zn. Concentration of observed (color-filled circles) and ANN-modeled (color map) dissolved Zn at upper (a) 100 m, (b) 400–600 m, and (c) 2,000–3,000 m. These maps visualize the mean of artificial neural networks (ANNs) ensemble and are produced using Ocean Data View (Schlitzer, 2015).

This dissolved Zn annual mean climatology (Figure 2) is applicable in open-ocean regions away from marginal and inland seas. The ability of the ANN to extrapolate outside of the open-ocean regions is limited. For example, the ANN is incapable of accurately predicting data in the Mediterranean and Black Seas, which were withheld from training, due to conditions in these basins (e.g., sulfidic conditions in the Black Sea) that are not found in the open-ocean. On the other hand, the ANN accurately predicts unseen data from the major ocean basins very well (Figure S4a).

### 2.5. Diagnostic Modeling

Maps of dissolved Zn produced from the ANNs, and climatological fields of  $\text{PO}_4^{3-}$  and  $\text{SiO}_4^{4-}$  (Garcia et al., 2014a, 2014b), are regridded and coupled to a transport matrix derived from an ocean circulation inverse

model (DeVries, 2014; resolution:  $2^\circ \times 2^\circ \times 24$  depth levels) to diagnose the net sources and sinks of these tracers. The equations of this diagnostic model are

$$\begin{bmatrix} \frac{d\mathbf{C}_s}{dt} \\ \frac{d\mathbf{C}_i}{dt} \end{bmatrix} = \begin{bmatrix} \mathbf{T}_{ss} & \mathbf{T}_{si} \\ \mathbf{T}_{is} & \mathbf{T}_{ii} \end{bmatrix} \begin{bmatrix} \mathbf{C}_s \\ \mathbf{C}_i \end{bmatrix} + \begin{bmatrix} \mathbf{J} \\ \mathbf{L} \end{bmatrix} = 0 \quad (1)$$

where  $\mathbf{T}_{ss}$ ,  $\mathbf{T}_{si}$ ,  $\mathbf{T}_{is}$ , and  $\mathbf{T}_{ii}$  (units of  $\text{yr}^{-1}$ ) are the partitions of the transport matrix that circulate the tracer  $\mathbf{C}$  (either Zn, P, or Si, units of concentration) from surface to surface, interior to surface, surface to interior, and interior to interior grid points, respectively. We define surface as the top 2 (upper 74 m) or 3 (upper 114 m) layers of the model grid.

$\mathbf{C}_s$  and  $\mathbf{C}_i$  are the tracer concentration at the surface and interior grid points, respectively.  $\mathbf{J}$  and  $\mathbf{L}$  are the net source-sink terms in the surface and interior, respectively.  $\mathbf{J}$  and  $\mathbf{L}$  are modeled using a restoring model:

$$\mathbf{J} = -\mathbf{J}_{\text{uptake}} = -\frac{F_{\text{rec}}(\mathbf{C}_s - \mathbf{C}_{s,\text{obs}})}{\tau} \quad (2)$$

$$\mathbf{L} = \mathbf{L}_{\text{reg}} = \frac{\mathbf{C}_{i,\text{obs}} - \mathbf{C}_i}{\tau} \quad (3)$$

where  $\mathbf{J}_{\text{uptake}}$  and  $\mathbf{L}_{\text{reg}}$  are the rates of uptake and regeneration, respectively, and  $\mathbf{C}_{s,\text{obs}}$  and  $\mathbf{C}_{i,\text{obs}}$  are the observed concentrations in the surface and interior, respectively.  $\tau$  is a restoring time-scale (1–9 months for uptake and 1–60 months for regeneration).  $F_{\text{rec}}$  is a rectifier function with the form of  $F_{\text{rec}}(x) = x \cdot \left(0.5 \cdot \tanh\left(\frac{x}{10^{-4}}\right) + 0.5\right)$ , applied exclusively on the uptake restoring model in order to allow only a net sink (uptake) in the surface. In the subsurface we allow both net positive and net negative regeneration rates, since both scavenging and regeneration can occur for dissolved Zn.

$\mathbf{J}_{\text{uptake}}$  is determined by inserting equation (2) into the upper row of equation (1) and replacing  $\mathbf{C}_i$  with the observed (or ANN-estimated) values of dissolved Zn,  $\text{SiO}_4^{4-}$  and  $\text{PO}_4^{3-}$  from the climatologies. The resulting equation is solved for  $\mathbf{C}_s$  and  $\mathbf{J}_{\text{uptake}}$ . Likewise,  $\mathbf{L}_{\text{reg}}$  is found by inserting equation (3) into equation (1) and replacing  $\mathbf{C}_s$  with the observed (or ANN-estimated) values of dissolved Zn,  $\text{SiO}_4^{4-}$  and  $\text{PO}_4^{3-}$ . The resulting equation is solved for  $\mathbf{C}_i$  and  $\mathbf{L}_{\text{reg}}$ .

The flux of particulate dissolved Zn,  $\text{SiO}_4^{4-}$ , and  $\text{PO}_4^{3-}$  (generally termed  $PC_{\text{flux}}$ ) can be reconstructed by integrating  $\mathbf{L}_{\text{reg}}$  over depth:

$$PC_{\text{flux}}(z) = \int_{z_{\text{bottom}}}^z \mathbf{L}_{\text{reg}} dz + PC_{\text{flux},z_{\text{bottom}}} \quad (4)$$

where  $z_{\text{bottom}}$  represents the depth of the seafloor. The actual flux calculation requires a known flux at a certain depth (i.e.,  $PC_{\text{flux},z_{\text{bottom}}}$ ). However, this only offsets the flux profile and does not change the shape of its variability with depth, which is our focus in this study. Hence, to have a consistent proxy of actual flux, we offset the fluxes to have the minima at zero. In most of the cases, these minima occur at the bottom grid point which means the fluxes should be close to the actual values if the flux of particles reaching the seafloor is negligible (which is a good assumption for, at least, particulate phosphorus).

Preformed components of dissolved Zn,  $\text{PO}_4^{3-}$ , and  $\text{SiO}_4^{4-}$  are calculated using equation (1) by setting  $\mathbf{C}_s$  (concentration within upper two layers of the circulation model) to observed values ( $\mathbf{C}_{s,\text{obs}}$ ) and assuming no sources or sinks in the interior ocean (i.e.,  $\mathbf{L} = 0$ ). The resulting equation is:

$$\mathbf{T}_{is}\mathbf{C}_{s,\text{obs}} + \mathbf{T}_{ii}\mathbf{C}_{i,\text{pre}} = 0 \quad (5)$$

The calculated preformed concentrations are then subtracted from the total observed concentrations to derive the regenerated concentrations,

$$\mathbf{C}_{\text{reg}} = \mathbf{C}_{\text{total}} - \mathbf{C}_{\text{pre}} \quad (6)$$

To simulate Zn distribution purely from the  $\text{PO}_4^{3-}$  regeneration and diagnosed  $\text{Zn}:\text{PO}_4^{3-}$  surface uptake ratio, we solve equation (1) by setting  $\mathbf{C}_s$  to our ANN-derived Zn concentration in the surface (upper two or three layers of the model), and  $\mathbf{L}$  as follows:

$$\mathbf{L} = \mathbf{L}_{\text{reg,PO}_4^{3-}} [\mathbf{Zn} : \text{PO}_4^{3-}]_{\text{Uptake,zonal}} \quad (7)$$

where  $\mathbf{L}_{\text{reg,PO}_4^{3-}}$  is our derived subsurface regeneration rate of  $\text{PO}_4^{3-}$  and  $[\mathbf{Zn}:\text{PO}_4^{3-}]_{\text{Uptake,zonal}}$  is our diagnosed  $\text{Zn}:\text{PO}_4^{3-}$  surface uptake ratio, when averaged zonally for each of Atlantic, Indian, and Pacific Oceans. By prescribing  $\mathbf{L}$  and  $\mathbf{C}_s$  in equation (1), we then solve the following equation for  $\mathbf{Zn}_{i, \text{from P}}$ , which is the concentration of Zn in the interior ocean that would occur if Zn were remineralized like P:

$$\mathbf{T}_{is} \mathbf{Zn}_{s, \text{obs}} + \mathbf{T}_{ii} \mathbf{Zn}_{i, \text{from P}} + \mathbf{L}_{\text{reg,PO}_4^{3-}} [\mathbf{Zn} : \text{PO}_4^{3-}]_{\text{Uptake,zonal}} = 0. \quad (8)$$

Finally, we define the *excess* regenerated Zn in the interior ocean as the difference between the calculated regenerated Zn (equation (6)) and the regenerated Zn that would occur if Zn remineralized like P:

$$\mathbf{Zn}_{i, \text{excess}} = \mathbf{Zn}_{\text{reg}} - \mathbf{Zn}_{i, \text{from P}}. \quad (9)$$

## 2.6. Assessing the Uncertainties

The calculations outlined above are performed 3,000 times for each tracer (dissolved Zn,  $\text{SiO}_4^{4-}$ , and  $\text{PO}_4^{3-}$ ) and each parameter of interest ( $\mathbf{J}_{\text{uptake}}$  and  $\mathbf{L}_{\text{reg}}$ ) through a Monte Carlo approach. For all calculations, we randomly select one of 10 versions of our circulation matrix ( $\mathbf{T}$ ; DeVries, 2014). For uptake calculations, we randomly choose a restoring time-scale ( $\tau$ ) in the range of 1–9 months. For regeneration, we randomly choose  $\tau$  to be in the range of 1–60 months. For the calculations using dissolved Zn, we randomly choose one out of the 100 fields produced by the ANN. For the definition of surface ocean, we randomly choose either the upper two layers (74 m) or two layers (114 m) of the model. All the above random parameters are drawn from uniform distributions. The discussion below is based on the mean and standard deviations of the calculated quantities (i.e., 100 dissolved Zn climatologies and 3,000 rate calculations).

## 3. Results and Discussion

### 3.1. The Global Zn Distribution

Our global climatology of dissolved Zn reveals elevated concentrations in the surface of the Southern Ocean of up to 5 nmol/kg (Figure 2a). The sub-Arctic Pacific is the only other open-ocean region with surface dissolved Zn concentration above 2 nmol/kg, while most of the rest of the surface ocean has concentrations below 1 nmol/kg (Figure 2a). At middepths we see accumulation of dissolved Zn in the North Pacific (8–10 nmol/kg) and Southern Ocean (6–8 nmol/kg; Figure 2b). The highest dissolved Zn concentrations are found in the deep ocean, particularly the North Pacific where concentrations exceed 10 nmol/kg (Figure 2c). In general, we see a typical nutrient-like increase of dissolved Zn along the *conveyor belt* circulation, with lowest concentrations in the North Atlantic Ocean ( $\text{Zn} < 4$  nmol/kg), intermediate concentrations in the Southern Ocean, and highest concentrations in the deep North Pacific (Figure 3a).

Correlations between the ANN-derived Zn climatology, and global climatologies of  $\text{SiO}_4^{4-}$  and  $\text{PO}_4^{3-}$ , are very similar to those derived from the observations (contours in Figures 1b and 1c). The ANN captures not only the strong correlation between dissolved Zn and  $\text{SiO}_4^{4-}$ , but also the much smaller deviations from the Zn- $\text{SiO}_4^{4-}$  correlation (termed Si-excess Zn;  $R^2 = 0.93$ , Figure S4b). These deviations are calculated as the difference between the observed (or ANN-predicted) dissolved Zn concentration, and the Zn concentration predicted by the linear relationship between Zn and  $\text{SiO}_4^{4-}$  (equation written on Figure 1b). The larger observed deviations from the global Zn- $\text{PO}_4^{3-}$  relationship (termed P-excess Zn; equation written on Figure 1c) are also well reproduced by the ANN ensemble ( $R^2 = 0.99$ ; Figure S4c).

The spatial patterns of Si-excess and P-excess Zn highlight differences between the cycling of Zn,  $\text{SiO}_4^{4-}$ , and  $\text{PO}_4^{3-}$  (Figures 3b and 3c). P-excess Zn gradually increases along the deep-ocean *conveyor belt* circulation from the North Atlantic to the North Pacific, acquiring largest positive values in the deep North Pacific (Figure 3b). Si-excess Zn in the deep ocean shows the opposite pattern, with positive values in the deep

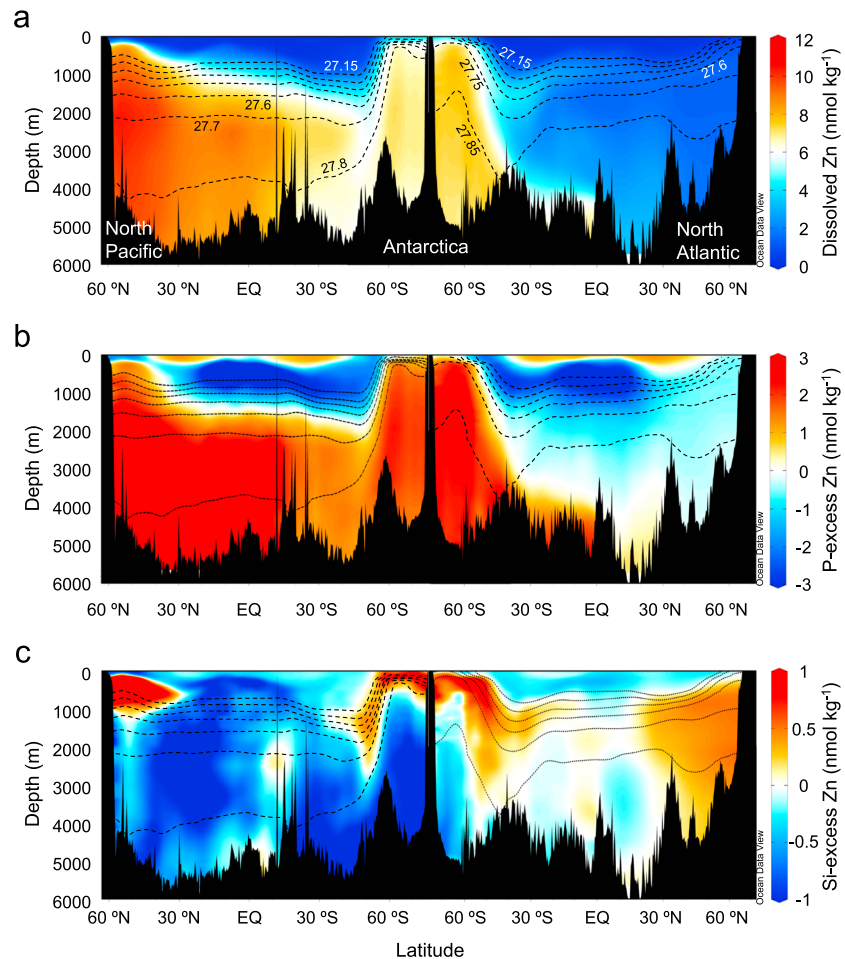


**Figure 3.** Sections of total dissolved and excess Zn. Distributions of ANN-derived total dissolved (a) Zn, (b) P-excess Zn, and (c) Si-excess Zn concentrations along meridional sections in the Atlantic (zonal average of 20–35°W) and Pacific (zonal average of 125–140°W) Oceans. Color maps were made using Ocean Data View (Schlitzer, 2015).

North Atlantic giving way to the most negative values in the deep Pacific (Figure 3c). These comparisons show that dissolved Zn is supplied to the deep ocean more efficiently than  $\text{PO}_4^{3-}$  but not as efficiently as  $\text{SiO}_4^{4-}$ .

Opposing patterns of P-excess and Si-excess Zn also occur at shallower depths. The most negative P-excess Zn values are found in the low-latitude thermocline throughout the ocean, while the most prominent regions of positive Si-excess Zn occur in the sub-Antarctic region of the Southern Ocean and in the middepth North Pacific. This pattern implies processes that deliver  $\text{PO}_4^{3-}$  more efficiently than Zn to the low-latitude thermocline and deliver Zn more efficiently than  $\text{SiO}_4^{4-}$  to high-latitude intermediate waters.

The patterns of P-excess and Si-excess Zn (Figures 3b and 3c) are driven by a combination of biological uptake in the surface ocean, regeneration and/or scavenging in the subsurface, and ocean circulation which propagates signals generated in one region to other regions. In order to separate the influence of each of these processes, we couple the ANN-derived dissolved Zn fields to a data-constrained global ocean circulation model (DeVries, 2014) and diagnose dissolved Zn uptake rates in the surface ocean, and regeneration rates in the subsurface ocean (see section 2.5). These calculations are repeated with  $\text{PO}_4^{3-}$  and  $\text{SiO}_4^{4-}$  in order to compare the cycling of Zn to that of the macronutrients.

### 3.2. Biological Uptake in the Surface Ocean

The diagnosed biological uptake rate of Zn varies with latitude. Relative to  $\text{PO}_4^{3-}$ , dissolved Zn uptake is enhanced in the high latitudes, particularly the Southern Ocean, where Zn:P (abbreviation for dissolved Zn

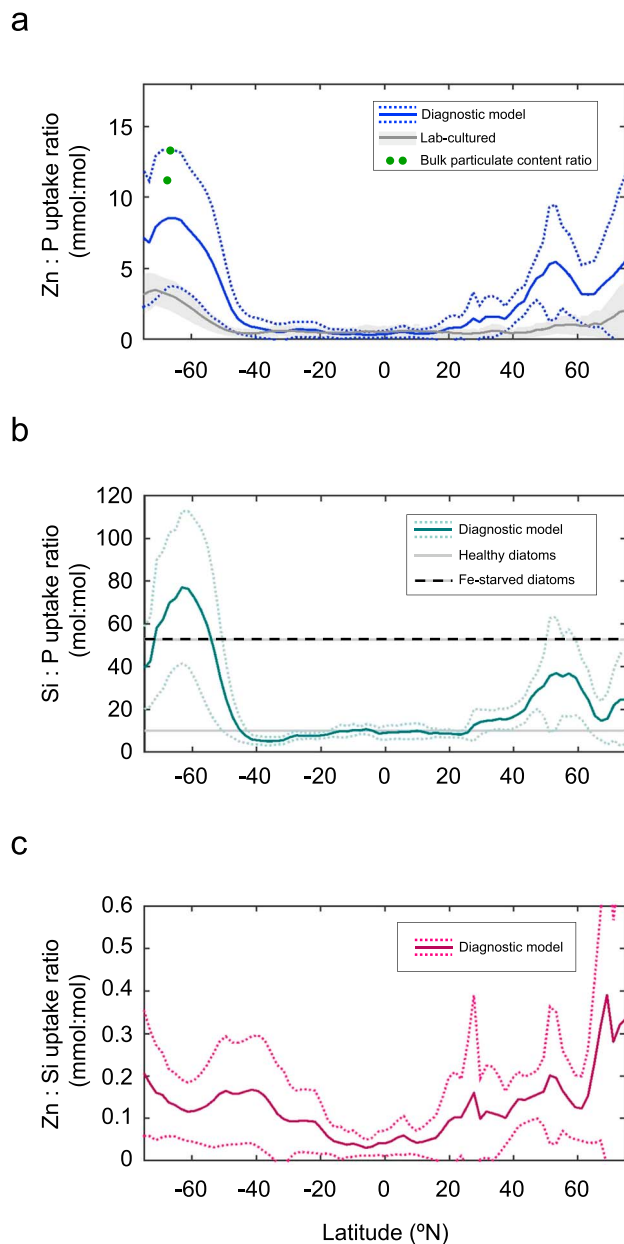


**Figure 4.** Surface uptake and particulate ratios. Zonally averaged diagnostically derived (a) Zn:P, (b) Si:P, and (c) Zn:Si uptake ratios. Also shown in panel a is the Zn:P uptake ratio calculated based on  $Zn^{2+}$ -dependent relationships from culture studies, applying a ligand concentration and stability constant of 0.5–2 nM and  $10^9$ – $10^{11}$  L/mol, respectively (Sunda & Huntsman, 2000; Twining & Baines, 2013). Bulk particulate Zn:P content ratios from field studies in the Southern Ocean are also shown in panel a (Collier & Edmond, 1984; Cullen et al., 2003). Si:P uptake ratios in healthy diatoms (solid gray line) and a maximal value for Fe-starved diatoms (dashed gray-black line; Hutchins & Bruland, 1998; Franck et al., 2000) are also shown in panel b.

to  $PO_4^{3-}$  uptake ratios exceed those in the low latitudes by more than tenfold (Figure 4a). The regions of high Zn:P uptake ratio coincide with high dissolved Zn concentrations (compare Figure 2a and Figure 4a), in agreement with laboratory culture experiments that show Zn:P uptake ratios increase with increasing Zn concentration (Sunda & Huntsman, 2000; Twining & Baines, 2013). However, the diagnosed Zn:P uptake ratios poleward of  $40^\circ S$  exceed those determined using plankton cultures at similar Zn concentrations (Figure 4a). Whereas plankton cultures predict Zn:P uptake ratios of  $\sim 2$ – $3$  (always in mmol:mol if omitted) at Zn concentrations similar to those found in the surface Southern Ocean, we find that the Zn:P uptake ratios can easily exceed 5 in the Southern Ocean and may reach values as high as 9–14, similar to the Zn:P content ratio measured in bulk particulate matter (Figure 4a; Collier & Edmond, 1984; Cullen et al., 2003). The Zn:P uptake ratio also exceeds 5:1 in the North Pacific, in contrast to the North Atlantic where Zn:P uptake ratios are  $\sim 2$ :1 (Figure S6a).

The predominance of diatoms could contribute to high Zn:P uptake ratios in the Southern Ocean. Diatoms have been shown to have higher Zn:P ratios than other plankton such as flagellates and picoplankton (Twining et al., 2004, 2011, 2015). However, this does not explain the large difference between the diagnosed Zn:P uptake ratios and those observed in laboratory diatom cultures. This difference could result from iron (Fe) limitation, which prevails in the high-latitude regions where we observe high Zn:P uptake ratios (Figures 4a and S6a; Martin & Fitzwater, 1988; Martin et al., 1990; Twining et al., 2004) and which reduces P uptake relative to Zn (Sunda & Huntsman, 2000). Supporting this idea, our diagnosed Si:P uptake ratios reveal that the Si:P uptake ratio steadily rises poleward of  $\sim 40^\circ S$  coincident with an increase in Zn:P uptake, reaching a maximum of  $\sim 80$ :1 mol:mol at  $\sim 60^\circ S$ , indicating uptake of Si by Fe-stressed diatoms (Figure 4b; Hutchins & Bruland, 1998; Franck et al., 2000). The Si:P ratio decreases poleward of  $\sim 60^\circ S$ , perhaps associated with higher Fe availability due to Fe input from the Antarctic continental shelf (de Jong et al., 2012).

We also diagnose a slightly elevated Zn:P uptake ratio in the subtropics, which can be seen most clearly in the subtropical gyres of the North Atlantic and North Pacific (Figure S6a). Enhanced Zn:P uptake in the subtropical gyres is probably related to the utilization of dissolved organic phosphorus, which has been shown to be an important source of P to phytoplankton in the  $PO_4^{3-}$ -limited North Atlantic subtropical gyre (Mather et al., 2008; Wu et al., 2000), and whose utilization is driven by a Zn-dependent Alkaline Phosphatase enzyme (Jakuba et al., 2008; Mahaffey et al., 2014; Shaked et al., 2006).

The Zn:Si uptake ratio of silicifying plankton (i.e., diatoms) is also highest in the Southern Ocean and the northern high latitudes (Figure 3c). Because the Zn:Si uptake ratio is high in both the North Pacific, which is Fe-limited, and North Atlantic, which is not (Figure S6c), we hypothesize that this ratio does not depend on Fe availability and could instead reflect the influence

of other trace metals such as cadmium (Cd), manganese (Mn) and cobalt (Co), low abundances of which can amplify Zn bio-assimilation (Sunda & Huntsman, 1995, 2000). Of these metals, dissolved Mn concentrations are lowest in the Southern Ocean (particularly south of  $58^\circ S$ ), while dissolved Cd and Co occur at moderate or even replete conditions (Baars et al., 2014; Bown et al., 2011; Middag et al., 2011). Another possible cause of the increased Zn:Si uptake at high latitudes is a lower concentration of Zn-binding ligands, which would

increase the ratio of bioavailable  $\text{Zn}^{2+}$  to total Zn concentration (Anderson & Morel, 1978; Brand et al., 1983; Bruland, 1989; Twining & Baines, 2013). As these ligands are a fraction, albeit small, of dissolved organic carbon, lower concentrations in the high latitudes are consistent with the general surface distribution of dissolved organic carbon (Roshan & DeVries, 2017). This ligand-associated mechanism would also cause an increase in the Zn:P uptake ratio above that found in laboratory cultures (Figure 4a).

Interestingly, the Zn:P uptake ratio of plankton does not correlate with the relative availability of dissolved Zn and  $\text{PO}_4^{3-}$  (Figure S7). In the high latitudes, Zn:P uptake ratios are higher than the corresponding concentration ratios; in low latitudes the situation is reversed (Figure S7; the same pattern is true of Zn:Si uptake and concentration ratios). In particular, we find that the Zn:P uptake ratio in the Antarctic and North Pacific regions are several factors higher than the concentration ratio (Figure S7). This situation could potentially lead the system to a Zn limitation if the plankton metabolism is not resilient to the lower dissolved Zn:P than is required for growth. However, the chronic Fe limitation in these areas probably overwhelms other potential limitations in the present-day ocean (Coale et al., 2003; Leblanc et al., 2005).

Overall, the results of our diagnostic model show that Fe limitation plays a significant role in controlling the Zn:P uptake ratio. Prognostic Zn cycling models should take into account the effect of Fe limitation on Zn:P uptake ratio, as well as the differences in the Zn requirements of different plankton. Other factors such as the abundance of Zn-binding ligands, the availability of other trace metals such as Cd and Mn, and the uptake of dissolved organic phosphorus may also play lesser roles in determining Zn:nutrient uptake ratios.

### 3.3. Particle Fluxes and Regeneration in the Deep Ocean

The global distribution of dissolved Zn in relation to the macronutrients is governed both by patterns of biological uptake and by the rates at which the exported biogenic material is regenerated in the subsurface ocean. To diagnose the role of subsurface regeneration in the dissolved Zn cycle, we calculate the subsurface source of dissolved Zn, Si, and P using a procedure similar to that used to calculate biological uptake (see section 2.5). These rates are then used to reconstruct the sinking fluxes of particulate Zn, biogenic silica, and phosphorus above 2,000 m (abbreviated as PZn, PSi, and PP, respectively; see section 2.5), assuming that the only sources and sinks between the base of the euphotic zone and 2,000 m are from particle regeneration and/or scavenging. This should hold approximately true, as the main external sources of Zn are in the surface ocean (rivers) and below 2,000 m (hydrothermal vents), while the primary sink of Zn is from burial on continental shelves, which are not resolved in our model (Little et al., 2014; Little et al., 2016; Roshan et al., 2016).

The Southern Ocean is the most important region for the production of biogenic Zn. The average profile of PZn flux in the Southern Ocean is strikingly similar to that of PP and contrasts strongly with that of PSi (Figure 5a). Fitting a power law or *Martin curve* of the form  $a(\text{depth})^{-b}$  to the reconstructed average particulate fluxes above 2,000 m, we find that the exponents of the PZn and PP fluxes are similar ( $0.53 \pm 0.04$  and  $0.67 \pm 0.07$ , respectively; uncertainties are those calculated during curve fitting on average profiles—that is, based on residuals), in contrast to the much smaller  $b$  value for PSi ( $0.28 \pm 0.02$ ; Figure 5a). These flux reconstructions indicate that biogenic Zn in the Southern Ocean is associated with plankton soft tissues containing P, rather than the Si-rich frustules of diatoms, a finding that agrees with the small percentage of Zn (1–3%) associated with frustules in laboratory diatom cultures (Ellwood & Hunter, 2000). A sediment trap study in the Southern Ocean ( $\sim 40^\circ\text{S}$ ) also found similar  $b$  values for PP and PZn, which were much higher than that derived for PSi (Twining et al., 2014).

Flux profiles of PZn and PP in the North Atlantic and North Pacific are also similar (Figures 5b and 5c). In each of these regions, the power law exponent of the particle flux attenuation with depth is similar for PZn and PP, and significantly larger than the  $b$  value for PSi (Figures 5b and 5c). Thus, the reconstructed flux profiles in all the high-latitude regions support the idea that PZn remineralizes as rapidly as PP, while PSi remains more preserved within the water column (Figures 5a to 5c). However, the only observational study of PZn fluxes in high latitudes outside the Southern Ocean, at a single station in the western North Pacific, calculated a PZn  $b$  value much lower than that of PP, and even PSi, in contrast to our results for the average North Pacific (Lamborg et al., 2008).

Low-latitude PZn fluxes are markedly different to those in the high latitudes (Figure 5d). In fact, in the low-latitude ocean PZn and PSi have very similar  $b$  values over the upper 2,000 m ( $0.15 \pm 0.11$  and  $0.22 \pm 0.26$ , respectively). This contrasts with the flux of PP, which attenuates more rapidly with depth in the low

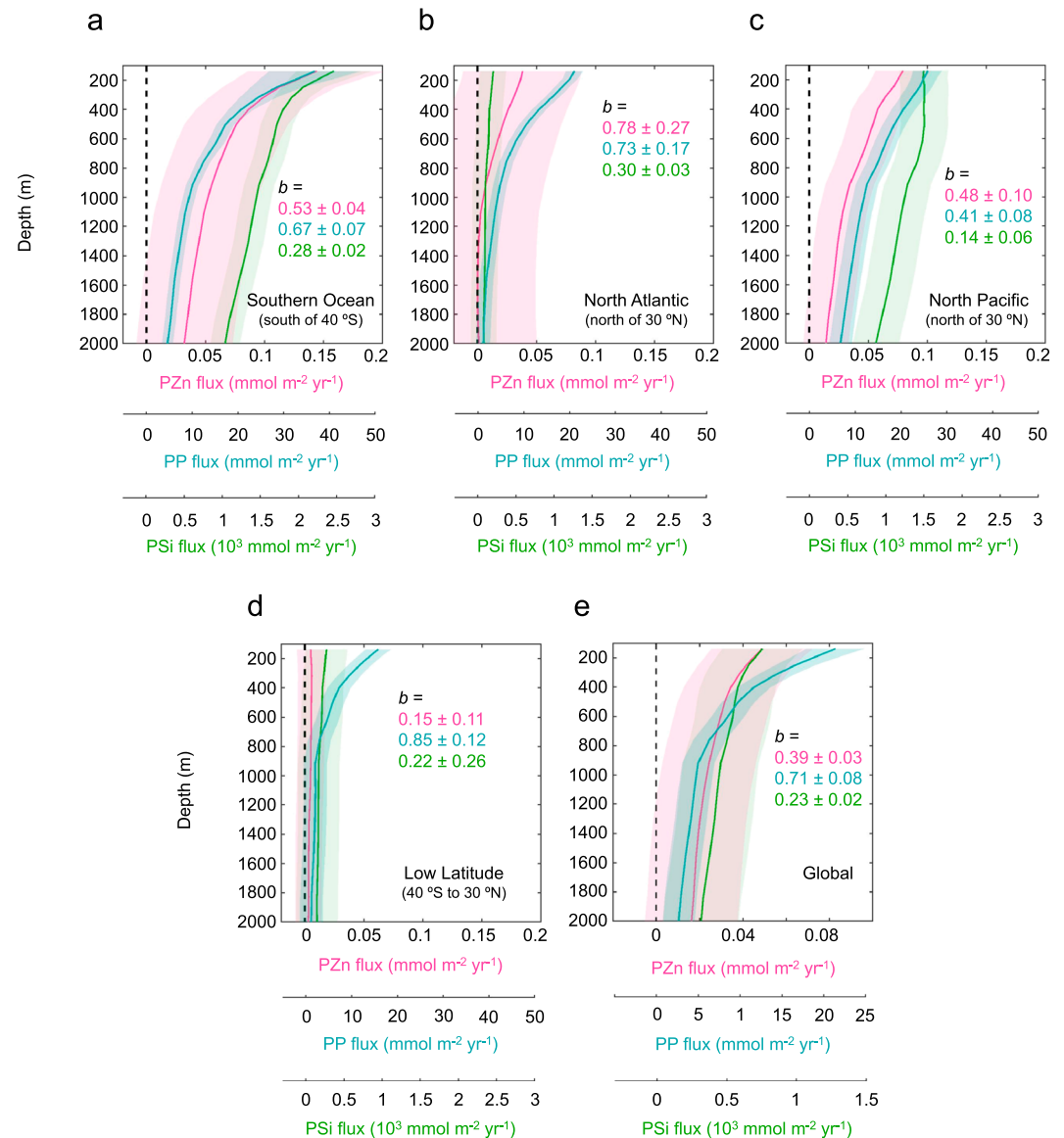


**Figure 5.** Fluxes of particulate Zn, Si and P. The average of particulate Zn (pink line plus shading indicating  $\pm 1$  standard deviation), Si (green), and P (cyan) in the upper 2,000 m of the (a) Southern Ocean (south of 40°S), (b) high-latitude North Atlantic (north of 30°N), (c) high-latitude North Pacific (north of 30°N), and (d) low-latitude global ocean (40°S–30°N). (e) Global average of particulate Zn, Si, and P fluxes. Also shown are the  $b$  values derived from a least squares fitting of  $a(\text{depth})^{-b}$  on the derived average particulate flux profiles, using the same color scheme as the flux profiles.

latitudes ( $b = 0.85 \pm 0.12$ ) than in the high latitudes, in agreement with a previous study (Weber et al., 2016). The slow attenuation of PZn fluxes in the low latitudes is consistent with the effects of reversible scavenging, which weakens the attenuation of particle fluxes with depth in low-flux environments (Weber et al., 2018). Although production of biogenic Zn is miniscule in the low latitudes, abundant sinking organic particles scavenge dissolved Zn out of seawater, sustaining a small but steady flux of PZn into the deep ocean.

The contrasting behavior of PZn fluxes in the high latitudes where PZn fluxes are dominated by biogenic Zn, and the low latitudes where PZn fluxes are dominated by scavenged Zn, leads to a globally averaged PZn flux profile that lies between that for PP and that for PSi, but more closely resembles the flux profile of biogenic Si due to the fact that the low latitudes have a greater area than the high latitudes (Figure 5e). The globally averaged  $b$  value in the upper 2,000 m for PZn ( $0.39 \pm 0.03$ ) is much smaller than that for PP ( $0.71 \pm 0.08$ ) but only slightly larger than that for PSi ( $0.23 \pm 0.02$ ).

Small and uncertain rates of regeneration in the deep ocean, as well as potential external sources of Zn from hydrothermal vents, make it difficult to calculate and compare the particle attenuation for depths below 2,000 m. In order to examine the source of dissolved Zn,  $\text{SiO}_4^{4-}$  and  $\text{PO}_4^{3-}$  in the deep ocean, we compare the accumulation of regenerated Zn,  $\text{SiO}_4^{4-}$  and  $\text{PO}_4^{3-}$  as a function of ventilation age in the deep ocean below 2,000 m (Figure 6a; the ventilation age is calculated using equation (1), taking into account the constraints:  $C_s = 0$ , and  $L = 1$  year/year. The second row of equation (1) is separated and solved for  $C_i$ , which, here, represents the water-mass ventilation age in the ocean interior.). We find that in the deep ocean regenerated Zn accumulates at a rate of  $2.9 (\pm 2.7)$  Gmol/year, while regenerated P accumulates at a rate of  $400 (\pm 72)$  Gmol/year and regenerated Si accumulates at a rate of  $66 (\pm 6)$  Tmol/year (Figure 6a).

The regeneration ratio of Zn:Si in the deep ocean is  $\sim 0.04:1$ , smaller than the global Zn:Si uptake ratio of  $\sim 0.1$ . This demonstrates that Zn is delivered less efficiently than Si to the deep ocean, consistent with the sharper flux attenuation of particulate Zn in those regions with high Zn fluxes (Figure 5). In contrast, there is an enhanced supply of regenerated Zn to the deep ocean over what would be expected just from the remineralization of P-associated organic Zn (compare the Zn:P deep-ocean regeneration ratio of  $\sim 7:1$  to the global Zn:P uptake ratio of  $\sim 2:1$ ), contributing to a buildup of P-excess Zn in the deep ocean (Figure 3b). This enhanced flux of Zn to the deep ocean appears to be partly driven by reversible scavenging (John & Conway, 2014; Weber et al., 2018), as evidenced by the particulate Zn flux profiles in low latitudes (Figure 5d), and partly driven by an input of Zn from hydrothermal vents, most of which occurs below 2,000 m and could add  $\sim 1.8$  Gmol Zn/year to the deep ocean (Roshan et al., 2016). Uncertainties in the magnitude of the hydrothermal Zn source to the deep ocean preclude accurate determination of the relative importance of reversible scavenging versus hydrothermal vents in supplying excess Zn to the deep ocean, but both processes are likely important.

Regardless of its source, this enhanced flux of Zn into the deep ocean increases Zn concentrations, helping to bring the deep-ocean Zn concentration closer to values expected from the observed tight Zn:Si correlation (Figure 6b). Indeed, our diagnostic model demonstrates that the Zn:Si correlation in the deep ocean is caused by not only a tight correlation of the preformed Zn:Si emanating mainly from the Southern Ocean but also a correlation of Zn and Si regenerated in subsurface waters, which accounts for the majority of Si and Zn in the deep ocean (Figure 6b).

Using our model, we explored what the deep-ocean Zn concentration would look like if Zn regenerated exactly like P, accounting for the large latitudinal variations in Zn:P uptake ratio in the surface ocean (see equation (8)). The resulting P-associated regenerated Zn distribution (Figure 6c) does not resemble the actual regenerated Zn distribution, and when added to the preformed Zn concentrations we find that the resulting total Zn concentration diverges substantially from the observations (Figure 6c inset). The difference between our diagnosed regenerated Zn concentration and the P-associated regenerated Zn concentration is termed the *excess regenerated Zn* (Figure 6c). The excess regenerated Zn is dissolved Zn that is delivered to the deep ocean by a combination of hydrothermal venting and reversible scavenging. This excess regenerated Zn is positive throughout most of the deep ocean but can be negative in young waters where scavenging is a significant sink of dissolved Zn. Excess regenerated Zn accumulates along with regenerated  $\text{SiOH}^{4-}$  (Figure 6c), contributing to the observed correlation between the two elements in the deep ocean.

### 3.4. A Schematic of the Global Ocean Zn Cycle

Our climatological dissolved Zn distribution and diagnostic model can be combined to present a complete picture of the oceanic Zn cycle and its relationship to that of P and Si (Figure 7). At the start of the global deep-ocean conveyor belt circulation in the North Atlantic, the concentration ratios of  $\text{SiO}_4^{4-}:\text{Zn}:\text{PO}_4^{3-}$  ( $\sim 19:1.5:1$ ) mainly reflect the preformed signature of North Atlantic Deep Waters (NADW; Figure 7). As deep waters age along the conveyor belt circulation, these ratios are substantially altered by the inflow of Antarctic Bottom Waters (AABW), and the flux of biogenic material originating from the Southern Ocean, which accounts for  $62 (\pm 32)\%$  of global Zn export, compared to  $58 (\pm 27)\%$  for  $\text{SiO}_4^{4-}$  and  $26 (\pm 12)\%$  for  $\text{PO}_4^{3-}$ . The combined effects of the regeneration of Zn- and Si-enriched biogenic matter, and the inflow of Zn- and Si-enriched AABW, raises the ratio of  $\text{SiO}_4^{4-}:\text{Zn}:\text{PO}_4^{3-}$  in deep Southern Ocean waters to  $\sim 51:3:1$  (Figure 7). While enriching the deep ocean in Zn relative to P, biological uptake in the Southern Ocean depletes northward flowing water-masses of Zn, causing low Zn:P ratios in Antarctic Intermediate Waters

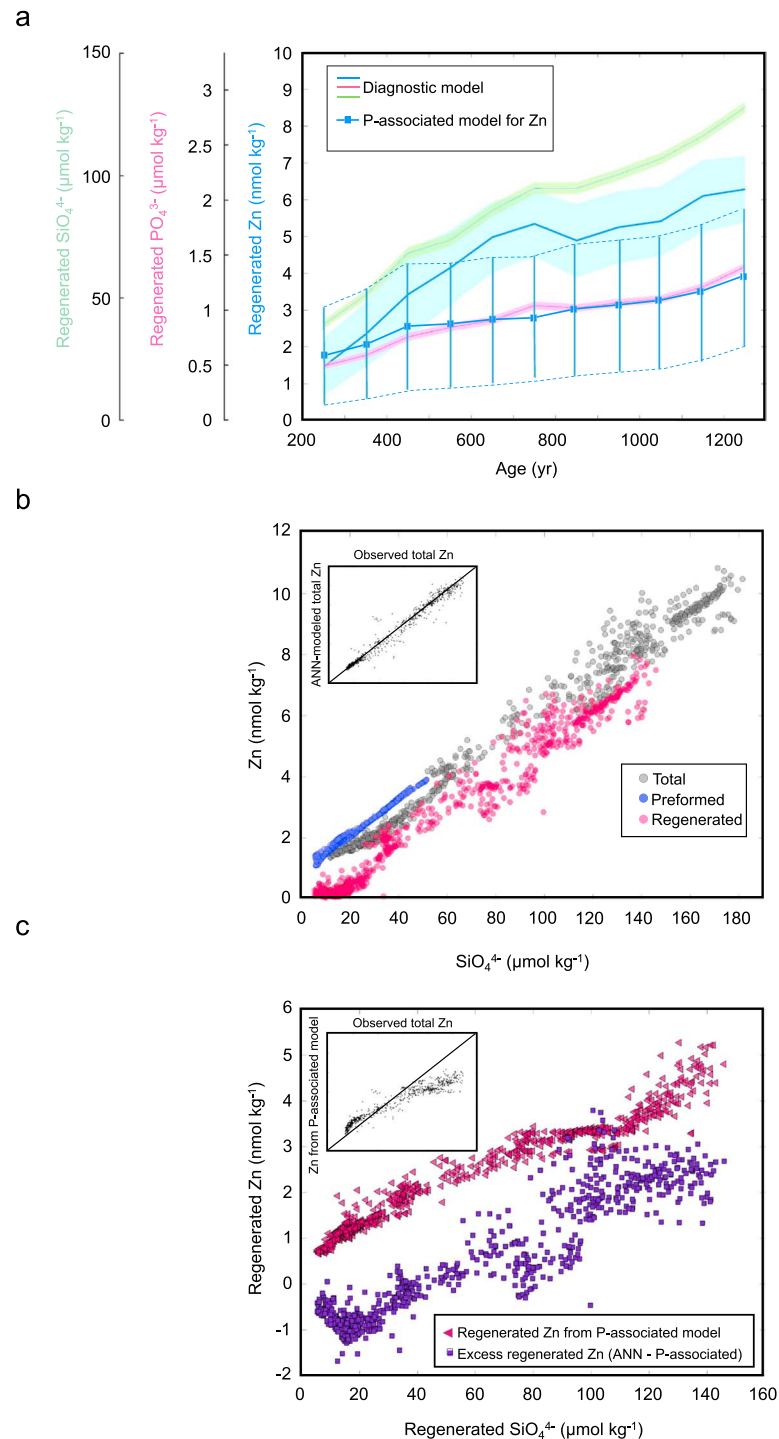


**Figure 6.** Trends of regenerated, preformed and total nutrients versus ideal age in the deep ocean. (a) Regenerated Zn,  $\text{PO}_4^{3-}$ , and  $\text{SiO}_4^{4-}$  (solid lines plus shading indicating  $\pm 1$  standard deviation), and the simulated P-associated regenerated Zn (see equation (8); solid line plus squares with bars and dashed lines indicating  $\pm 1$  standard deviation), in the deep global ocean ( $>2,000$  m) as averaged within 100-year age bins. (b) Total, preformed and regenerated Zn against those of  $\text{SiO}_4^{4-}$  at locations in the deep ocean that have dissolved Zn observations. The inset plot in panel b shows the total Zn from our ANN climatology against observed total Zn. (c) P-associated regenerated Zn (red triangles; see equation (8)), and the difference between total regenerated Zn and P-associated regenerated Zn (excess regenerated Zn; purple squares; calculated using equation (9)) versus regenerated  $\text{SiO}_4^{4-}$ . The inset plot in panel c shows the total Zn assuming that all regenerated Zn is P-associated. Note that the calculation of P-associated regenerated Zn takes into account the latitudinally varying  $\text{Zn}:\text{PO}_4^{3-}$  uptake ratio in the surface ocean (see equation (8)).

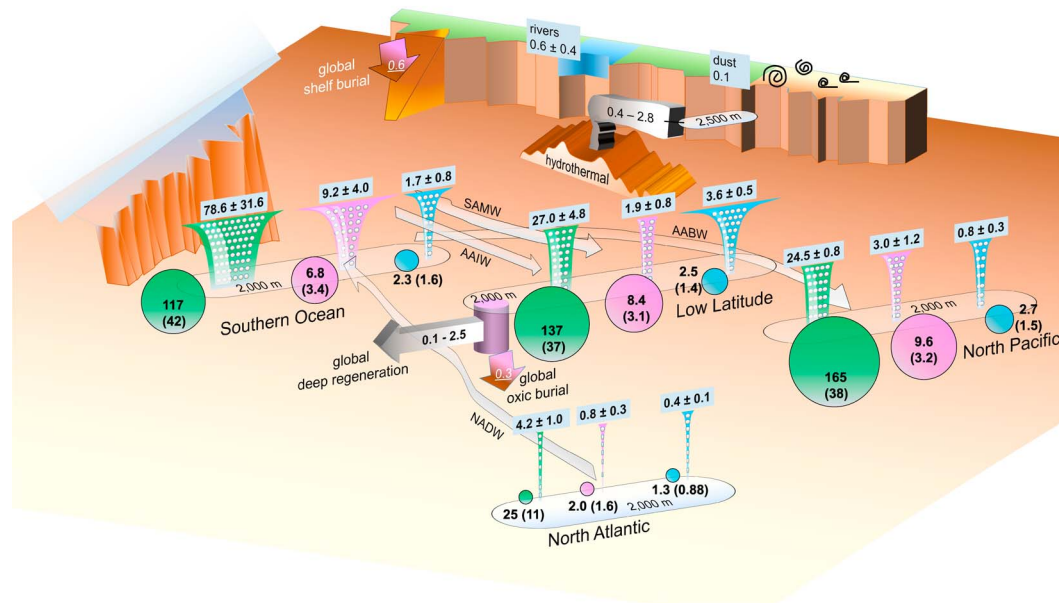


**Figure 7.** Global cycling of Zn in the ocean. This schematic shows the internal particle-associated cycling of Zn in the ocean, as well as some recent estimates of the external sources and sinks of Zn. Particulate Zn, Si, and P fluxes in the regions according to Figure 5 are visualized as pink, green, and cyan funnels, respectively, with values on top of each showing their exports out of the surface ocean as particles (units are Gmol/year for Zn and Tmol/year for Si and P, and uncertainties are  $\pm 1$  standard deviation). The sizes of the circles show the relative mean concentration of total and preformed (within the parentheses) Zn (pink; nmol/kg),  $\text{SiO}_4^{4-}$  (green;  $\mu\text{mol/kg}$ ), and  $\text{PO}_4^{3-}$  (cyan;  $\mu\text{mol/kg}$ ) below 2,000 m in each of the regions. Rates of boundary inputs and sinks (underlined) of Zn are also shown in Gmol/year. Also shown is a schematic of water mass flows including North Atlantic Deep Water (NADW), Antarctic Bottom Water (AABW), Antarctic Intermediate Water (AAIW), and Sub-Antarctic Mode Water (SAMW).

(AAIW) and sub-Antarctic Mode Waters (SAMW; Figure 7). These Zn-depleted water masses feed production in the low-latitude oceans, accounting for the low Zn fluxes from the low latitudes (Figure 7).

Despite the weak biological uptake of Zn in low latitudes, a protracted flux of Zn into the deep ocean driven by reversible scavenging, along with input from hydrothermal vents, preserves the high Zn concentration in deep waters, leading to a  $\text{SiO}_4^{4-}:\text{Zn}:\text{PO}_4^{3-}$  ratio of  $\sim 55:3.4:1$  in the low-latitude deep Pacific and Indian Oceans. This ratio increases further in the North Pacific, where there is substantial export of biogenic Zn fed by the upwelling of Zn-enriched deep waters (Figure 7).

Large uncertainties remain in the mechanisms responsible for delivering Zn to the deep ocean. We diagnose a source of Zn to the deep ocean of  $2.9 (\pm 2.7)$  Gmol/year. Combining measurements of excess Zn in hydrothermal plumes of the southeastern Pacific (Roshan et al., 2016) with recent estimates of hydrothermal  $^3\text{He}$  inputs (Holzer et al., 2017) yields hydrothermal Zn inputs to the deep ocean of  $0.4\text{--}2.8$  Gmol/year. The remaining  $0.1\text{--}2.5 (\pm 2.7)$  Gmol/year originates from the regeneration of PZn, including a source from the desorption of dissolved Zn that has been scavenged by particles (Weber et al., 2018).

Previous Zn budgets put the burial of Zn in oxic (deep-ocean) sediments at  $0.3$  Gmol/year (Little et al., 2014), indicating that most of the Zn added to the deep ocean is upwelled to the surface where it fuels biological productivity. Any Zn from hydrothermal vents must thus be buried on continental shelves to balance the Zn budget, but current estimates of Zn burial on continental shelves can only accommodate the lower end of our estimated hydrothermal Zn input (Little et al., 2016). This points toward a need to improve estimates of Zn input from hydrothermal vents by making more dissolved Zn measurements within hydrothermal plumes.

### 3.5. Uncertainties and Possible Improvements

Remaining uncertainties in the oceanic Zn cycle can be addressed with improved data coverage, improved data interpolation techniques, and higher fidelity ocean circulation state estimates. The Southern Ocean

should be a high-priority target for future observational studies, as the uncertainties in our interpolated dissolved Zn concentrations are particularly large in this data-poor but globally critical region. Likewise, we have considered one variant of machine-learning methods (ANNs) to interpolate the sparse dissolved Zn concentrations, but it is possible that other variants of machine/deep learning methods could be employed to better extract information from the limited dissolved Zn data. Finally, we have used a data-assimilated ocean circulation inverse model with high fidelity to observed distributions of physical tracers (DeVries, 2014), but nonetheless, there remain uncertainties in the circulation state estimate related to the coarse spatial resolution of the model, neglect of seasonal variability, and sensitivity of the circulation to prescribed subgridscale diffusivities. Future studies will benefit from data-assimilated circulations at higher spatial resolution, and that resolve seasonal variability in circulation. The methods presented in this study provide a *pipeline* for incorporating future iterations of data and models, through which we can steadily refine our understanding of the global ocean Zn cycle.

#### 4. Conclusion

Our study gives a complete picture of the ocean Zn cycle, demonstrating both similarities and difference between the cycles of Zn and macronutrients. The Zn and Si cycles are mechanistically coupled through the uptake of Zn and Si by diatoms in the Southern Ocean, where biological uptake of Zn is further enhanced by Fe scarcity. But the relationship between Si and Zn that is set by uptake in the Southern Ocean is slowly eroded in the subsurface by particle regeneration, which occurs shallower for Zn and P and deeper for Si, so that without an additional process adding Zn to the deep ocean the Zn concentration would drift away from that of Si. Reversible scavenging and hydrothermal Zn inputs both appear to be important sources of excess Zn to the deep ocean, helping to maintain a tight relationship between Zn and Si. Since Si has no hydrothermal source and is not reversibly scavenged, the correlation of Zn and Si in the modern ocean is in large part coincidental. Different ocean circulation states are likely to exhibit entirely different Zn-Si relationships.

#### Acknowledgments

This work was supported by NASA award NNX122G and NSF grant OCE-1658392 to T. D. and by NSF grants OCE-1233155 and CNSF grant 41776092 to J. W. The compiled observational data set and ANN-produced climatology of dissolved zinc are publically available at <https://doi.org/10.6084/m9.figshare.7403627.v3>.

#### References

- Anderson, M. A., & Morel, F. M. M. (1978). Growth limitation of a coastal diatom by low zinc ion activity. *Nature*, 276(5683), 70–71. <https://doi.org/10.1038/276070a0>
- Baars, O., Abouchami, W., Galer, S. J., Boye, M., & Croot, P. L. (2014). Dissolved cadmium in the Southern Ocean: Distribution, speciation, and relation to phosphate. *Limnology and Oceanography*, 59(2), 385–399. <https://doi.org/10.4319/lo.2014.59.2.0385>
- Bacon, M. P., & Anderson, R. F. (1982). Distribution of thorium isotopes between dissolved and particulate forms in the deep sea. *Journal of Geophysical Research*, 87(C3), 2045–2056. <https://doi.org/10.1029/JC087iC03p02045>
- Bown, J., Boye, M., Baker, A., Duvieilbourg, E., Lacan, F., Le Moigne, F., et al. (2011). The biogeochemical cycle of dissolved cobalt in the Atlantic and the Southern Ocean south off the coast of South Africa. *Marine Chemistry*, 126(1–4), 193–206. <https://doi.org/10.1016/j.marchem.2011.03.008>
- Brand, L. E., Sunda, W. G., & Guillard, R. R. (1983). Limitation of marine phytoplankton reproductive rates by zinc, manganese, and iron. *Limnology and Oceanography*, 28(6), 1182–1198. <https://doi.org/10.4319/lo.1983.28.6.1182>
- Bruland, K. W. (1980). Oceanographic distributions of cadmium, zinc, nickel, and copper in the north pacific. *Earth and Planetary Science Letters*, 47(2), 176–198. [https://doi.org/10.1016/0012-821X\(80\)90035-7](https://doi.org/10.1016/0012-821X(80)90035-7)
- Bruland, K. W. (1989). Complexation of zinc by natural organic ligands in the central North Pacific. *Limnology and Oceanography*, 34(2), 269–285. <https://doi.org/10.4319/lo.1989.34.2.0269>
- Bruland, K. W., Middag, R., & Lohan, M. C. (2014). Controls of trace metals in seawater. In H. Holland & K. Turekian (Eds.), *Treatise on geochemistry* (2nd ed., Vol. 8, pp. 19–51). Oxford: Elsevier.
- Bruland, K. W., Orians, K. J., & Cowen, J. P. (1994). Reactive trace metals in the stratified central North Pacific. *Geochimica et Cosmochimica Acta*, 58(15), 3171–3182. [https://doi.org/10.1016/0016-7037\(94\)90044-2](https://doi.org/10.1016/0016-7037(94)90044-2)
- Coale, K. H., Wang, X., Tanner, S. J., & Johnson, K. S. (2003). Phytoplankton growth and biological response to iron and zinc addition in the Ross Sea and Antarctic Circumpolar Current along 170°W. *Deep Sea Research Part II: Topical Studies in Oceanography*, 50(3–4), 635–653. [https://doi.org/10.1016/S0967-0645\(02\)00588-X](https://doi.org/10.1016/S0967-0645(02)00588-X)
- Collier, R., & Edmond, J. (1984). The trace element geochemistry of marine biogenic particulate matter. *Progress in Oceanography*, 13(2), 113–199. [https://doi.org/10.1016/0079-6611\(84\)90008-9](https://doi.org/10.1016/0079-6611(84)90008-9)
- Croot, P. L., Baars, O., & Streu, P. (2011). The distribution of dissolved zinc in the Atlantic sector of the Southern Ocean. *Deep Sea Research Part II: Topical Studies in Oceanography*, 58(25–26), 2707–2719. <https://doi.org/10.1016/j.dsr2.2010.10.041>
- Cullen, J. T., Chase, Z., Coale, K. H., Fitzwater, S. E., & Sherrell, R. M. (2003). Effect of iron limitation on the cadmium to phosphorus ratio of natural phytoplankton assemblages from the Southern Ocean. *Limnology and Oceanography*, 48(3), 1079–1087. <https://doi.org/10.4319/lo.2003.48.3.1079>
- de Jong, J., Schoemann, V., Lannuzel, D., Croot, P., de Baar, H., & Tison, J. L. (2012). Natural iron fertilization of the Atlantic sector of the Southern Ocean by continental shelf sources of the Antarctic Peninsula. *Journal of Geophysical Research*, 117, G01029. <https://doi.org/10.1029/2011JG001679>
- de Souza, G. F., Khaliwala, S. P., Hain, M. P., Little, S. H., & Vance, D. (2018). On the origin of the marine zinc–silicon correlation. *Earth and Planetary Science Letters*, 492, 22–34.

- DeVries, T. (2014). The oceanic anthropogenic CO<sub>2</sub> sink: Storage, air-sea fluxes, and transports over the industrial era. *Global Biogeochemical Cycles*, 28, 631–647. <https://doi.org/10.1002/2013GB004739>
- Ellwood, M. J., & Hunter, K. A. (2000). The incorporation of zinc and iron into the frustule of the marine diatom *Thalassiosira pseudonana*. *Limnology and Oceanography*, 45(7), 1517–1524. <https://doi.org/10.4319/lo.2000.45.7.1517>
- Fitzwater, S. E., Johnson, K. S., Gordon, R. M., Coale, K. H., & Smith, W. O. (2000). Trace metal concentrations in the Ross Sea and their relationship with nutrients and phytoplankton growth. *Deep Sea Research Part II: Topical Studies in Oceanography*, 47(15-16), 3159–3179. [https://doi.org/10.1016/S0967-0645\(00\)00063-1](https://doi.org/10.1016/S0967-0645(00)00063-1)
- Franck, V. M., Brzezinski, M. A., Coale, K. H., & Nelson, D. M. (2000). Iron and silicic acid concentrations regulate Si uptake north and south of the polar frontal zone in the Pacific sector of the Southern Ocean. *Deep Sea Research Part II: Topical Studies in Oceanography*, 47(15-16), 3315–3338. [https://doi.org/10.1016/S0967-0645\(00\)00070-9](https://doi.org/10.1016/S0967-0645(00)00070-9)
- Garcia, H. E., Locarnini, R. A., Boyer, T. P., Antonov, J. I., Baranova, O. K., Zweng, M. M., et al. (2014a). In S. Levitus & A. Mishonov (Eds.), *World ocean atlas 2013, Volume 3: Dissolved oxygen, apparent oxygen utilization, and oxygen saturation*, NOAA Atlas NESDIS 75 (p. 27). Silver Spring, MD: US Government Printing Office.
- Garcia, H. E., Locarnini, R. A., Boyer, T. P., Antonov, J. I., Baranova, O. K., Zweng, M. M., et al. (2014b). In S. Levitus & A. Mishonov (Eds.), *World ocean atlas 2013, Volume 4: Dissolved inorganic nutrients (phosphate, nitrate, silicate)*, NOAA Atlas NESDIS 76 (p. 25). Silver Spring, MD: US Government Printing Office.
- Hassoun, M. H. (1995). *Fundamentals of artificial neural networks*. Cambridge, MA: MIT Press.
- Holzer, M., DeVries, T., Bianchi, D., Newton, R., Schlosser, P., & Winckler, G. (2017). Objective estimates of mantle <sup>3</sup>He in the ocean and implications for constraining the deep ocean circulation. *Earth and Planetary Science Letters*, 458, 305–314. <https://doi.org/10.1016/j.epsl.2016.10.054>
- Holzer, M., Primeau, F. W., DeVries, T., & Matear, R. (2014). The Southern Ocean silicon trap: Data-constrained estimates of regenerated silicic acid, trapping efficiencies, and global transport paths. *Journal of Geophysical Research: Oceans*, 119, 313–331. <https://doi.org/10.1002/2013JC009356>
- Hutchins, D. A., & Bruland, K. W. (1998). Iron-limited diatom growth and Si:N uptake ratios in a coastal upwelling regime. *Nature*, 393(6685), 561–564. <https://doi.org/10.1038/31203>
- Jakuba, R. W., Moffett, J. W., & Dyhrman, S. T. (2008). Evidence for the linked biogeochemical cycling of zinc, cobalt, and phosphorus in the western North Atlantic Ocean. *Global Biogeochemical Cycles*, 22, GB4012. <https://doi.org/10.1029/2007GB003119>
- Janssen, D. J., & Cullen, J. T. (2015). Decoupling of zinc and silicic acid in the subarctic Northeast Pacific interior. *Marine Chemistry*, 177, 124–133. <https://doi.org/10.1016/j.marchem.2015.03.014>
- John, S. G., & Conway, T. M. (2014). A role for scavenging in the marine biogeochemical cycling of zinc and zinc isotopes. *Earth and Planetary Science Letters*, 394, 159–167. <https://doi.org/10.1016/j.epsl.2014.02.053>
- John, S. G., Helgoe, J., & Townsend, E. (2018). Biogeochemical cycling of Zn and Cd and their stable isotopes in the eastern tropical South Pacific. *Marine Chemistry*, 201, 256–262. <https://doi.org/10.1016/j.marchem.2017.06.001>
- Kim, T., Obata, H., Nishioka, J., & Gamo, T. (2017). Distribution of dissolved zinc in the western and central subarctic North Pacific. *Global Biogeochemical Cycles*, 31, 1454–1468. <https://doi.org/10.1002/2017GB005711>
- Lamborg, C. H., Buesseler, K. O., & Lam, P. J. (2008). Sinking fluxes of minor and trace elements in the North Pacific Ocean measured during the VERTIGO program. *Deep Sea Research Part II: Topical Studies in Oceanography*, 55(14-15), 1564–1577. <https://doi.org/10.1016/j.dsr2.2008.04.012>
- Lauvset, S. K., Key, R. M., Olsen, A., van Heuven, S., Velo, A., Lin, X., et al. (2016). A new global interior ocean mapped climatology: the 1° × 1° GLODAP version 2. *Earth System Science Data*, 8, 325–340.
- Leblanc, K., Hare, C. E., Boyd, P. W., Bruland, K. W., Sohst, B., Pickmere, S., et al. (2005). Fe and Zn effects on the Si cycle and diatom community structure in two contrasting high and low-silicate HNLC areas. *Deep Sea Research Part I: Oceanographic Research Papers*, 52(10), 1842–1864. <https://doi.org/10.1016/j.dsr.2005.06.005>
- Little, S. H., Vance, D., McManus, J., & Severmann, S. (2016). Key role of continental margin sediments in the oceanic mass balance of Zn and Zn isotopes. *Geology*, 44, 207–210.
- Little, S. H., Vance, D., Walker-Brown, C., & Landing, W. M. (2014). The oceanic mass balance of copper and zinc isotopes, investigated by analysis of their inputs, and outputs to ferromanganese oxide sediments. *Geochimica et Cosmochimica Acta*, 125, 673–693. <https://doi.org/10.1016/j.gca.2013.07.046>
- Locarnini, R. A., Mishonov, A. V., Antonov, J. I., Boyer, T. P., Garcia, H. E., Baranova, O. K., et al. (2013). In S. Levitus & A. Mishonov (Eds.), *World ocean atlas 2013, Volume 1: Temperature*, NOAA Atlas NESDIS 73 (p. 40). Silver Spring, MD: US Government Printing Office.
- Mahaffey, C., Reynolds, S., Davis, C. E., & Lohan, M. C. (2014). Alkaline phosphatase activity in the subtropical ocean: Insights from nutrient, dust and trace metal addition experiments. *Frontiers in Marine Science*, 1, 73.
- Martin, J. H., & Fitzwater, S. E. (1988). Iron deficiency limits phytoplankton growth in the north-east Pacific subarctic. *Nature*, 331(6154), 341–343. <https://doi.org/10.1038/331341a0>
- Martin, J. H., Fitzwater, S. E., & Gordon, R. M. (1990). Iron deficiency limits phytoplankton growth in Antarctic waters. *Global Biogeochemical Cycles*, 4(1), 5–12. <https://doi.org/10.1029/GB004i001p00005>
- Martin, J. H., Fitzwater, S. E., Gordon, R. M., Hunter, C. N., & Tanner, S. J. (1993). Iron, primary production and carbon-nitrogen flux studies during the JGOFS North Atlantic Bloom Experiment. *Deep Sea Research Part II: Topical Studies in Oceanography*, 40(1–2), 115–134. [https://doi.org/10.1016/0967-0645\(93\)90009-C](https://doi.org/10.1016/0967-0645(93)90009-C)
- Martin, J. H., Gordon, R. M., Fitzwater, S., & Broenkow, W. W. (1989). VERTX: Phytoplankton/iron studies in the Gulf of Alaska. *Deep Sea Research*, 36(5), 649–680. [https://doi.org/10.1016/0198-0149\(89\)90144-1](https://doi.org/10.1016/0198-0149(89)90144-1)
- Mather, R. L., Reynolds, S. E., Wolff, G. A., Williams, R. G., Torres-Valdes, S., Woodward, E. M. S., et al. (2008). Phosphorus cycling in the North and South Atlantic Ocean subtropical gyres. *Nature Geoscience*, 1(7), 439–443. <https://doi.org/10.1038/ngeo232>
- Mawji, E., Schlitzer, R., Dodas, E. M., Abadie, C., Abouchami, W., Anderson, R. F., et al. (2015). The GEOTRACES intermediate data product 2014. *Marine Chemistry*, 177, 1–8. <https://doi.org/10.1016/j.marchem.2015.04.005>
- Middag, R., De Baar, H. J. W., Laan, P., Cai, P. H., & Van Ooijen, J. C. (2011). Dissolved manganese in the Atlantic sector of the Southern Ocean. *Deep Sea Research Part II: Topical Studies in Oceanography*, 58(25-26), 2661–2677. <https://doi.org/10.1016/j.dsr2.2010.10.043>
- Morel, A., Huot, Y., Gentili, B., Werdell, P. J., Hooker, S. B., & Franz, B. A. (2007). Examining the consistency of products derived from various ocean color sensors in open ocean (Case 1) waters in the perspective of a multi-sensor approach. *Remote Sensing of Environment*, 111(1), 69–88. <https://doi.org/10.1016/j.rse.2007.03.012>
- Roshan, S., & DeVries, T. (2017). Efficient dissolved organic carbon production and export in the oligotrophic ocean. *Nature Communications*, 8(1), 2036. <https://doi.org/10.1038/s41467-017-02227-3>

- Roshan, S., DeVries, T., Wu, J., & Chen, G. (2018). Dissolved zinc climatology (Version 3). figshare. <https://doi.org/10.6084/m9.figshare.7403627.v3>
- Roshan, S., & Wu, J. (2015). Water mass mixing: The dominant control on the zinc distribution in the North Atlantic Ocean. *Global Biogeochemical Cycles*, 29, 1060–1074. <https://doi.org/10.1002/2014GB005026>
- Roshan, S., Wu, J., & Jenkins, W. J. (2016). Long-range transport of hydrothermal dissolved Zn in the tropical South Pacific. *Marine Chemistry*, 183, 25–32. <https://doi.org/10.1016/j.marchem.2016.05.005>
- Sauzède, R., Bittig, H. C., Claustre, H., Pasquero de Fommervault, O., Gattuso, J. P., Legendre, L., & Johnson, K. S. (2017). Estimates of water-column nutrient concentrations and carbonate system parameters in the global ocean: A novel approach based on neural networks. *Frontiers in Marine Science*, 4, 128. <https://doi.org/10.3389/fmars.2017.00128>
- Schlitzer, R. (2015). Ocean Data View. Retrieved from <http://odv.awi.de>
- Schlitzer, R., Anderson, R. F., Dodas, E. M., Lohan, M., Geibert, W., Tagliabue, A., et al. (2018). The GEOTRACES intermediate data product 2017. *Chemical Geology*, 493, 210–223. <https://doi.org/10.1016/j.chemgeo.2018.05.040>
- Shaked, Y., Xu, Y., Leblanc, K., & Morel, F. M. M. (2006). Zinc availability and alkaline phosphatase activity in *Emiliania huxleyi*: Implications for Zn-P co-limitation in the ocean. *Limnology and Oceanography*, 51(1), 299–309. <https://doi.org/10.4319/lo.2006.51.1.0299>
- Sunda, W. G., & Huntsman, S. A. (1995). Cobalt and zinc interreplacement in marine phytoplankton: Biological and geochemical implications. *Limnology and Oceanography*, 40(8), 1404–1417. <https://doi.org/10.4319/lo.1995.40.8.1404>
- Sunda, W. G., & Huntsman, S. A. (2000). Effect of Zn, Mn, and Fe on Cd accumulation in phytoplankton: Implications for oceanic Cd cycling. *Limnology and Oceanography*, 45(7), 1501–1516. <https://doi.org/10.4319/lo.2000.45.7.1501>
- Twining, B. S., & Baines, S. B. (2013). The trace metal composition of marine phytoplankton. *Annual Review of Marine Science*, 5(1), 191–215. <https://doi.org/10.1146/annurev-marine-121211-172322>
- Twining, B. S., Baines, S. B., Bozard, J. B., Vogt, S., Walker, E. A., & Nelson, D. M. (2011). Metal quotas of plankton in the equatorial Pacific Ocean. *Deep Sea Research Part II: Topical Studies in Oceanography*, 58(3–4), 325–341. <https://doi.org/10.1016/j.dsr2.2010.08.018>
- Twining, B. S., Baines, S. B., & Fisher, N. S. (2004). Element stoichiometries of individual plankton cells collected during the Southern Ocean Iron Experiment (SOFEX). *Limnology and Oceanography*, 49(6), 2115–2128. <https://doi.org/10.4319/lo.2004.49.6.2115>
- Twining, B. S., Nodder, S. D., King, A. L., Hutchins, D. A., LeClerc, G. R., DeBruyn, J. M., et al. (2014). Differential remineralization of major and trace elements in sinking diatoms. *Limnology and Oceanography*, 59(3), 689–704. <https://doi.org/10.4319/lo.2014.59.3.0689>
- Twining, B. S., Rauschenberg, S., Morton, P. L., & Vogt, S. (2015). Metal contents of phytoplankton and labile particulate material in the North Atlantic Ocean. *Progress in Oceanography*, 137, 261–283. <https://doi.org/10.1016/j.pocean.2015.07.001>
- Vance, D., Little, S. H., de Souza, G. F., Khatiwala, S., Lohan, M. C., & Middag, R. (2017). Silicon and zinc biogeochemical cycles coupled through the Southern Ocean. *Nature Geoscience*, 10(3), 202–206. <https://doi.org/10.1038/ngeo2890>
- Weber, T., Cram, J. A., Leung, S. W., DeVries, T., & Deutsch, C. (2016). Deep ocean nutrients imply large latitudinal variation in particle transfer efficiency. *Proceedings of the National Academy of Sciences of the United States of America*, 113(31), 8606–8611. <https://doi.org/10.1073/pnas.1604414113>
- Weber, T., John, S., Tagliabue, A., & DeVries, T. (2018). Biological uptake and reversible scavenging of zinc in the global ocean. *Science*, 361(6397), 72–76. <https://doi.org/10.1126/science.aap8532>
- Wu, J., Sunda, W., Boyle, E. A., & Karl, D. M. (2000). Phosphate depletion in the western North Atlantic Ocean. *Science*, 289(5480), 759–762. <https://doi.org/10.1126/science.289.5480.759>
- Wyatt, N. J., Milne, A., Woodward, E. M. S., Rees, A. P., Browning, T. J., Bouman, H. A., et al. (2014). Biogeochemical cycling of dissolved zinc along the GEOTRACES South Atlantic transect GA10 at 40 S. *Global Biogeochemical Cycles*, 28, 44–56. <https://doi.org/10.1002/2013GB004637>
- Zhao, Y., Vance, D., Abouchami, W., & de Baar, H. J. (2014). Biogeochemical cycling of zinc and its isotopes in the Southern Ocean. *Geochimica et Cosmochimica Acta*, 125, 653–672. <https://doi.org/10.1016/j.gca.2013.07.045>
- Zweng, M. M., Reagan, J. R., Antonov, J. I., Locarnini, R. A., Mishonov, A. V., Boyer, T. P., et al. (2013). In S. Levitus & A. Mishonov (Eds.), *World ocean atlas 2013, Volume 2: Salinity, NOAA Atlas NESDIS 74* (p. 39). Silver Spring, MD: US Government Printing Office.